

Soft X-ray Imager of the Xtend system onboard *XRISM* *

Hirofumi Noda¹, Koji Mori^{2,3}, Hiroshi Tomida³, Hiroshi Nakajima^{4,3}, Takaaki Tanaka⁵, Hiroshi Murakami⁶, Hiroyuki Uchida⁷, Hiromasa Suzuki³, Shogo Benjamin Kobayashi⁸, Tomokage Yoneyama⁹, Kouichi Hagino¹⁰, Kumiko Nobukawa¹¹, Hideki Uchiyama¹², Masayoshi Nobukawa¹³, Hironori Matsumoto¹⁴, Takeshi Go Tsuru⁷, Makoto Yamauchi², Isamu Hatsukade², Hirokazu Odaka¹⁴, Takayoshi Kohmura¹⁵, Kazutaka Yamaoka¹⁶, Tessei Yoshida³, Yoshiaki Kanemaru³, Junko Hiraga¹⁷, Tadayasu Dotani³, Masanobu Ozaki¹⁸, Hiroshi Tsunemi¹⁴, Jin Sato², Toshiyuki Takaki², Yuta Terada², Keitaro Miyazaki², Kohei Kusunoki², Yoshinori Otsuka², Haruhiko Yokosu², Wakana Yonemaru², Kazuhiro Ichikawa², Hanako Nakano², Reo Takemoto², Tsukasa Matsushima², Reika Urase², Jun Kurashima², Kotomi Fuchi², Kaito Hayakawa⁴, Masahiro Fukuda⁴, Takamitsu Kamei⁴, Yoh Asahina⁴, Shun Inoue⁷, Amano Yuki³, Yuma Aoki¹¹, Yamato Ito¹¹, Tomoya Kamatani¹¹, Kouta Takayama¹¹, Takashi Sako¹³, Marina Yoshimoto¹⁴, Kohei Shima¹⁴, Mayu Higuchi¹⁵, Kaito Ninoyu¹⁵, Daiki Aoki¹⁵, Shun Tsunomachi¹⁵, and Kiyoshi Hayashida¹⁴

¹Astronomical Institute, Tohoku University, 6-3 Aramaki-zaaoba, Aoba-ku, Sendai, Miyagi 980-8578, Japan

²Faculty of Engineering, University of Miyazaki, 1-1 Gakuen Kibanadai Nishi, Miyazaki, Miyazaki 889-2192, Japan

³Japan Aerospace Exploration Agency, Institute of Space and Astronautical Science, 3-1-1 Yoshino-dai, Chuo-ku, Sagami-hara, Kanagawa 252-5210, Japan

⁴College of Science and Engineering, Kanto Gakuin University, Kanazawa-ku, Yokohama, Kanagawa 236-8501, Japan

⁵Department of Physics, Konan University, 8-9-1 Okamoto, Higashinada, Kobe, Hyogo 658-8501

⁶Faculty of Informatics, Tohoku Gakuin University, 3-1 Shimizukoji, Wakabayashi-ku, Sendai, Miyagi 984-8588

⁷Department of Physics, Kyoto University, Kitashirakawa Oiwake-cho, Sakyo-ku, Kyoto, Kyoto 606-8502, Japan

⁸Department of Physics, Faculty of Science, Tokyo University of Science, Kagurazaka, Shinjuku-ku, Tokyo 162-0815, Japan

⁹Faculty of Science and Engineering, Chuo University, 1-13-27 Kasuga, Bunkyo-ku, Tokyo 112-8551, Japan

¹⁰Department of Physics, University of Tokyo, 7-3-1 Hongo, Bunkyo-ku, Tokyo 113-0033, Japan

¹¹Department of Physics, Kindai University, 3-4-1 Kowakae, Higashi-Osaka, Osaka 577-8502, Japan

¹²Science Education, Faculty of Education, Shizuoka University, Suruga-ku, Shizuoka, Shizuoka 422-8529, Japan

¹³Faculty of Education, Nara University of Education, Nara, Nara 630-8528, Japan

¹⁴Department of Earth and Space Science, Osaka University, 1-1 Machikaneyama-cho, Toyonaka, Osaka 560-0043, Japan

¹⁵Department of Physics, Faculty of Science and Technology, Tokyo University of Science, 2641 Yamazaki, Noda, Chiba 270-8510, Japan

¹⁶Department of Physics, Nagoya University, Chikusa-ku, Nagoya, Aichi 464-8602, Japan

¹⁷Department of Physics, Kwansei Gakuin University, 2-2 Gakuen, Sanda, Hyogo 669-1337, Japan

¹⁸Advanced Technology Center, National Astronomical Observatory of Japan, Mitaka, Tokyo 181-8588, Japan

*E-mail: hirofumi.noda@astr.tohoku.ac.jp

Abstract

The Soft X-ray Imager (SXI) is the X-ray charge-coupled device (CCD) camera for the soft X-ray imaging telescope Xtend installed on the *X-ray Imaging and Spectroscopy Mission (XRISM)*, which was adopted as a recovery mission for the *Hitomi* X-ray satellite and was successfully launched on 2023 September 7 (JST). In order to maximize the science output of *XRISM*, we set the requirements for Xtend and find that the CCD set employed in the *Hitomi*/SXI or similar, i.e., a 2×2 array of back-illuminated CCDs with a $200 \mu\text{m}$ -thick depletion layer, would be practically best among available choices, when used in combination with the X-ray mirror assembly. We design the *XRISM*/SXI, based on the *Hitomi*/SXI, to have a wide field of view of $38' \times 38'$ in the 0.4–13 keV energy range. We incorporated several significant improvements from the *Hitomi*/SXI into the CCD chip design to enhance the optical-light blocking capability and to increase the cosmic-ray tolerance, reducing the degradation of charge-transfer efficiency in orbit. By the time of the launch of *XRISM*, the imaging and spectroscopic capabilities of the SXI has been extensively studied in on-ground experiments with the full flight-model configuration or equivalent setups and confirmed to meet the requirements. The optical blocking capability, the cooling and temperature control performance, and the transmissivity and quantum efficiency to incident X-rays of the CCDs are also all confirmed to meet the requirements. Thus, we successfully complete the pre-flight development of the SXI for *XRISM*.

Keywords: instrumentation: detectors — techniques: imaging spectroscopy — methods: data analysis — vehicles: instruments — X-rays:

general

1 Introduction

X-ray Imaging and Spectroscopy Mission (XRISM) (Tashiro et al. 2018; 2020; 2024) is the seventh Japanese X-ray astronomical satellite, adopted as the recovery mission of the short-lived *ASTRO-H (Hitomi)* satellite (Takahashi et al. 2018). Its development commenced in 2017, and it was successfully launched by the H-IIA rocket F47 from the JAXA Tanegashima Space Center on 2023 September 7 (JST). Although its predecessor *Hitomi* was lost about a month after its launch on 2016 February 17 due to attitude-control troubles, it demonstrated during its short lifetime the power of ultra-precise X-ray spectroscopy on multiple astrophysical objects with an X-ray microcalorimeter for the first time. Most notably, the observations of the Perseus cluster of galaxies revealed the detailed velocity and temperature distributions, heavy element composition of its hot plasma, and structure of an active galactic nucleus (AGN) at its center with an unprecedented precision (e.g., Hitomi Collaboration 2016; 2017; 2018a; 2018b; 2018c). Considering the significance and uniqueness of X-ray spectroscopy of cosmic sources in an ultra-high energy resolution, it was first decided that *Hitomi*'s recovery mission, *XRISM*, should be equipped with a soft X-ray spectroscopy telescope ‘‘Resolve,’’ a system with an X-ray microcalorimeter combined with thin foiled conically approximated Wolter-I mirror optics with a focal length of 5.6 m (X-ray Mirror Assembly; XMA).

The downside of Resolve is a relatively narrow field of view (FOV) of $3' \times 3'$ and a large pixel size of $30''$, which is larger than the size at the core of the Point-Spread Function (PSF) of the XMA. The mission team decided to employ on *XRISM* a complementary instrument for wider-FOV, finer, and more precise imaging in the same energy band. For this purpose, a wide FOV X-ray imager with a small pixel size and low Non X-ray Background (NXB) level is essential. Accordingly, it was decided that the soft X-ray imaging telescope ‘‘Xtend,’’ a system with an X-ray charge-coupled device (CCD) camera named ‘‘Soft X-ray Imager’’ (SXI) combined with a separate XMA from that for Resolve would also be installed on *XRISM* (namely, Xtend = SXI + XMA; Hayashida et al. 2018; Nakajima et al. 2020; Mori et al. 2022; Mori et al. 2024). The design of the SXI is based on the CCD camera of the predecessor *Hitomi* (which was also called the SXI; see Section 2), but some significant improvements are made, as explained in detail in this paper.

This paper presents the description of the SXI of the Xtend system onboard *XRISM* and its basic characteristics, organized as follows. Section 2 gives the requirements for Xtend. Section 3 explains the design of the SXI with a particular emphasis on design improvements from the *Hitomi*/SXI. Section 4 describes the on-board and on-ground event processing. Section 5 shows the SXI's performances measured with experiments with the full flight-model configuration and equivalent setups. Note that the known issues of anomalous charge intrusion on the CCD chips of the same model but non-flight-model ones and the countermeasures for the issues are reported in the separate paper by Noda et al. (2024). The in-orbit performance of the *XRISM*/Xtend/SXI will be also reported in a separate paper.

2 Requirements for Xtend

The following list summarizes the desired features of Xtend with the aim of maximizing the science outputs by *XRISM*.

1. Enhancement of the potentials of spectroscopy in an unprecedentedly high energy resolution with Resolve, including the reduction of non-target-source contamination and noise
 - (a) When a point source is present in the FOV of Resolve together with a diffuse source extending beyond the FOV of Resolve, (e.g., an AGN at the center of a cluster of galaxies), Xtend can distinguish their spectra by utilizing signals outside the FOV of Resolve.
 - (b) Even if a bright transient appears outside the FOV of Resolve and a part of its flux contaminates the main target signals within the FOV, Xtend can evaluate and exclude the flux contamination precisely, taking account of its energy dependence.
 - (c) The combination of Xtend and Resolve enhances continuum-emission statistics with an increase of a signal-to-noise ratio by a factor of $\sim \sqrt{2}$ for a point source and up to an order of magnitude for a diffuse source (while the gate valve of Resolve remains open¹). The fact that the two detectors cover almost the same energy band is an advantage for this.
 - (d) In modeling highly extended diffuse sources beyond the field of view, be it in the foreground (e.g., Solar-wind charge exchange emission) or background (e.g., Galactic diffuse sources), Xtend's much wider FOV yields much higher statistics than those with Resolve, hence providing much higher statistics for their data.
 - (e) Some operations and calibrations in orbit cannot be completed by Resolve alone and require Xtend, such as the confirmation of a pointing direction, the calibration of the PSF, and the molecular contamination monitoring necessary prior to the operation of opening the gate valve of Resolve.
2. Soft X-ray spectroscopic imaging with the wide FOV of Xtend with a low NXB level
 - (a) Xtend is particularly effective for studying widely extended diffuse sources, such as the outer regions of galaxy clusters, supernova remnants, Galactic ridge X-ray emission, superbubbles, and the Warm-Hot Intergalactic Medium (WHIM), outperforming higher-NXB X-ray instruments.
 - (b) Although the coverage of sky with Xtend is greatly limited compared with all-sky monitors such as *MAXI*, its sensitivity is ~ 4 orders of magnitude higher than *MAXI*, and the FOV is significantly wider than most other modern X-ray imaging instruments such as *Chandra*/ACIS and *XMM-Newton*/EPIC.

Then, the following requirements were set for Xtend to satisfy the desired features.

- As a focal-plane X-ray sensor, a back-illuminated CCD chip is

¹ In the first year of operation of *XRISM* in orbit (2023–2024), the gate valve of Resolve remained closed, which had maintained vacuum in the dewar on ground and was planned to be opened before the normal operation phase began. The gate valve in the closed position blocks a significant part of incoming X-rays to the X-ray microcalorimeter of Resolve, by $\sim 40\%$ in effective area even at relatively-high 6 keV and much worse in the lower energy bands, up to virtually 100% below 1.7 keV. As a result, Xtend/SXI's role has turned out to be even more significant than the pre-launch expectation, given that Resolve has so far had a much reduced effective area in the lower energy band.

* The corresponding authors are Hirofumi Noda, Koji Mori, Hiroshi Tomida, Hiroshi Nakajima, Takaaki Tanaka, and Hiroshi Murakami.

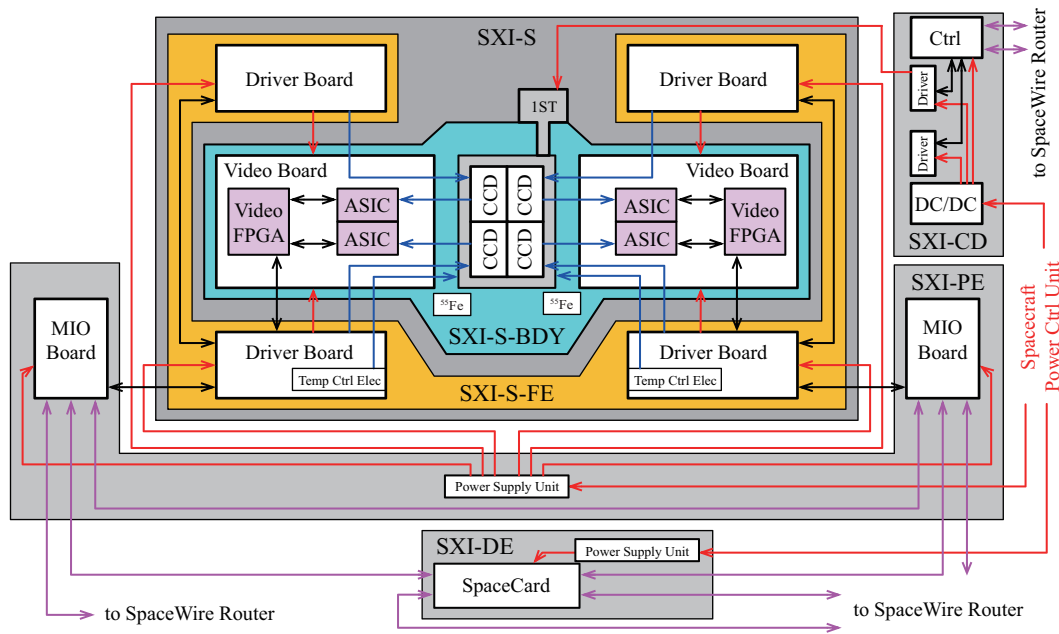


Fig. 1. Block diagram of the *XRISM/SXI* system, modified from the diagram of the *Hitomi/SXI* system in Tanaka et al. (2018). Red, blue, purple, and black lines show the power supply, analog, SpaceWire, and notable digital signal flows, respectively. Alt text: One block diagram.

superior, considering the overall balance, notably its high tolerance to micrometeoroids and orbital debris.

- The FOV must be larger than $22' \times 22'$ for feature items 1-(a, b, d) and 2-(a, b) in the list above.
- The effective area must be larger than 300 cm^2 at 1.5 keV and larger than 270 cm^2 at 6 keV for feature items 1-(a, b, c, d) and 2-(a, b).
- The pixel size must be below $100 \mu\text{m}$, with which the PSF core of the XMA (Tamura et al. 2022) can be spatially resolved (1-(e)).
- The detector must be sensitive for the energy range from 0.4 to 13 keV to cover almost the same range as Resolve (1-(a, b, c, d) and 2-(b)).
- The energy resolution at 6 keV must be better than 200 eV in Full Width Half Maximum (FWHM) at the Beginning-Of-Life (BOL) and 250 eV (FWHM) at the End-Of-Life (EOL) (1-(d) and 2-(a)).
- The optical blocking performance (light reduction) must be $< 10^{-13}$ along the X-ray light path including the reduction by (the structure of) the satellite itself of 10^{-6} (1-(a, b, c, d) and 2-(a, b)).
- The NXB level must be below $1 \times 10^{-6} \text{ counts keV}^{-1} \text{ s}^{-1} \text{ arcmin}^{-2} \text{ cm}^{-1}$ in 5–10 keV (1-(a, d) and 2-(a, b)).

We found that the best solution that satisfies all these requirements was a combination of the XMA and the CCD-chip model “PchNeXT4” fabricated by Hamamatsu Photonics K.K (Matsuura et al. 2006; Ozawa et al. 2006; Takagi et al. 2006; Ueda et al. 2011; Ueda et al. 2013). The PchNeXT4 chip is a P-channel Back-Illuminated (BI)-type CCD with a 200- μm -thick depletion layer. Four chips of the type were employed in the X-ray CCD camera onboard *Hitomi* (Tanaka et al. 2018), which is also called the SXI, and their performances have already been studied well on ground and in orbit (Nakajima et al. 2018). For the

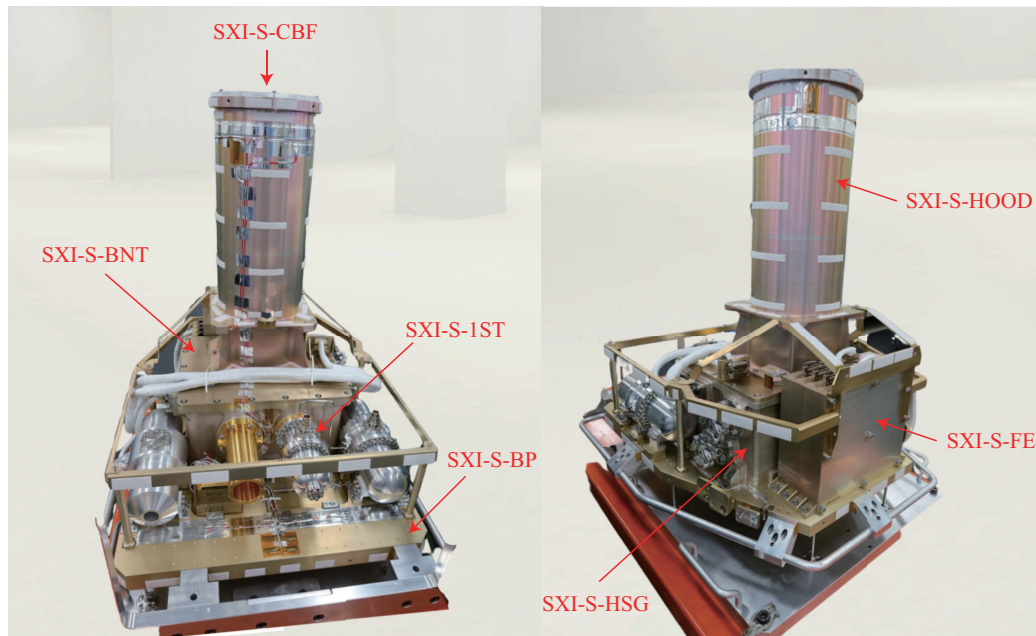
XRISM/Xtend/SXI, we developed a variant of PchNeXT4, applying some improvements that we considered desirable after examining the in-orbit performance of the original PchNeXT4 chips, and named the new CCD chips “PchNeXT4A.” The next section §3 provides a detailed description of the improvements that we made. For the *XRISM/Xtend/SXI*, we arranged four PchNeXT4A chips in a 2×2 array. As shown from the next section, the *XRISM/Xtend/SXI* can be considered one of the best X-ray CCD cameras ever installed on X-ray astronomical satellites, offering a relatively large FOV with a stable NXB level and achieving the largest grasp at 7 keV among X-ray CCD cameras onboard large observatories when combined with the XMA (see Uchida et al. in prep for the in-orbit performance of Xtend). Hereafter, we refer to the SXI of the Xtend system onboard *XRISM* as the *XRISM/SXI* or just SXI, and the SXI onboard *Hitomi* as the *Hitomi/SXI*, to distinguish them clearly.

3 Design of the *XRISM/SXI*

Figure 1 shows a block diagram of the *XRISM/SXI*. The *XRISM/SXI* is composed of four parts of the sensor part (SXI-S), the pixel processing electronics (SXI-PE), the digital electronics (SXI-DE), and the cooler driver (SXI-CD), in the same way as in the design of and naming convention for the *Hitomi/SXI* (Tanaka et al. 2018). In this section, we present a brief summary of each part (refer to the design description of the *Hitomi/SXI* presented in Tanaka et al. (2018) for detail), except for the changes that we made from the *Hitomi/SXI*, for which we give a full description here. Table 1 summarizes the changes in one sentence for each. Most of the components described in this section are manufactured by Mitsubishi Heavy Industry, Ltd., while the CCD chips were fabricated by Hamamatsu Photonics K.K, as mentioned in §2, and the others were provided by JAXA. Mitsubishi Heavy Industry, Ltd. assembled them into the SXI.

Table 1. Summary of the design changes from the *Hitomi*/SXI to *XRISM*/SXI.

Component	Design change	Reason for the change	Section
CCD chips	Thickness of the OBL	To prevent light leakage through pinholes	§3.1.2
	Additional Al layer	To prevent light leakage via the physical edges	§3.1.2
	Notch implant	To suppress the charge transfer inefficiency	§3.1.2
SXI-S-1ST	Reduction of one of the two 1STs	Based on the <i>Hitomi</i> /SXI performance	§3.1.5
SXI-PE	Reduction of clocking modes	Based on the necessity in orbit	§3.2.2

**Fig. 2.** Photographs of the (left panel) front and (right) back sides of SXI-S (credit: JAXA). Alt text: Two photographs.

3.1 Sensors and front-end components: SXI-S

Figure 2 shows an overall picture of SXI-S, which is a sensor part at the focal plane of the XMA, located on the base plate of the spacecraft. SXI-S consists of the camera body (SXI-S-BDY; §3.1.1), single-stage Stirling cooler (SXI-S-1ST; §3.1.5), video boards (§3.1.3), and four driver boards (SXI-S-FE; §3.1.4). The CCD driving clock patterns, operating commands, and heater control commands are provided to SXI-S from SXI-PE, whereas the driving power of SXI-S-1ST is independently input from SXI-CD. CCD image data and House Keeping (HK) data are digitized in the video and driver boards of SXI-S and then transferred to SXI-PE.

3.1.1 Camera body: SXI-S-BDY

The camera body, SXI-S-BDY, is made of Al alloy (Figure 2). In this subsection, we describe the relative positions of the components of SXI-S-BDY in the orientation in which the SXI observes X-rays from sources located directly *above* SXI-S-BDY as in Figure 2. The main components of SXI-S-BDY are a focal plane assembly (SXI-S-FPA), housing (SXI-S-HSG), bonnet (SXI-S-BNT), hood (SXI-S-HOOD), contamination blocking filter (SXI-S-CBF), vent pipes (SXI-S-VP), and base plate (SXI-S-BP).

SXI-S-BNT is a lid set at the top of SXI-S-HSG. SXI-S-HOOD is a baffle set above SXI-S-BNT to block stray X-rays without sac-

rificing a wide FOV. SXI-S-CBF is installed at the top of SXI-S-HOOD and spatially separates inside and outside of SXI-S-BDY to block contamination. The design of SXI-S-CBF is the same as that of the *Hitomi*/SXI, i.e., a 200-nm polyamide layer is sandwiched by 80-nm and 40-nm Al layers (n.b., the presented thicknesses are design values). SXI-S-FPA consists of four CCD chips of PchNeXT4A (see §3.1.2), a cold plate with heaters, video boards (see §3.1.3), and mechanical support structure inside SXI-S-HSG. SXI-S-VP is composed of two vent pipes for venting remaining gases in SXI-S-BDY outside the spacecraft. SXI-S-BP is positioned approximately ten centimeters above the base plate of the spacecraft using Ti alloy shafts, preventing distortion due to thermal expansion and minimizing thermal interaction between SXI-S and the spacecraft through conduction. Multi-Layer Insulators (MLIs) cover SXI-S-BDY, which suppresses heat exchange by radiation. The heat produced in SXI-S is carried to the radiators through heat pipes connected to the SXI-S-BP. For a countermeasure to molecular contamination inside SXI-S-BDY, we baked every component at $\sim 100^\circ\text{C}$ before the launch until the amount of outgas became lower than the detection limit. With this baking process, the amount of molecular contamination absorbed onto the surfaces of the CCDs from SXI-S-BDY should remain $< 4 \mu\text{g}/\text{cm}^2$ after 3 years in-orbit operation (i.e., until the EOL) according to our model estimate.

Two calibration sources of ^{55}Fe radioisotopes are placed at the

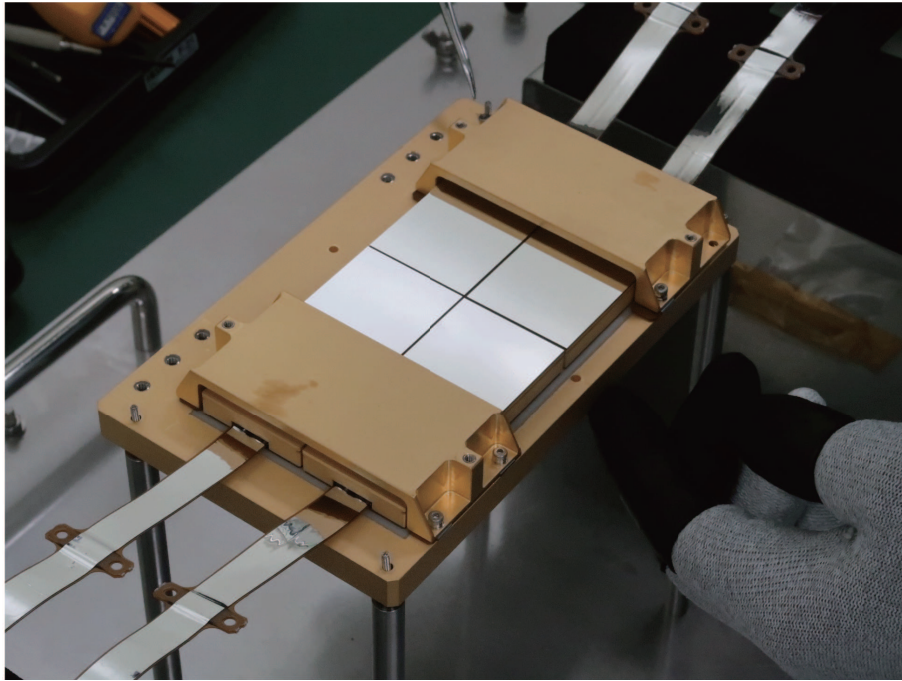


Fig. 3. Photograph of the flight-model CCD chips mounted on the cold plate. The four CCD chips are mounted on the cold plate supported by jigs. The frame-store regions of the CCD sensors are shielded by the frame-store cover, and a Flexible Printed Circuit (FPC) extends from each of the four CCD sensors. Alt text: One photograph.

surface of SXI-S-BNT above the CCD chips to measure the imaging and spectroscopic performance of the SXI in orbit. X-ray photons from the calibration sources are irradiated to the corners of the four CCD chips, and each irradiated region is a circular quadrant with a radius smaller than 4.5 mm. To determine the energy gain at 5.9 keV within 0.1% accuracy, the count rate of 0.4 counts/sec/CCD is required. Considering a half-life of ^{55}Fe of 2.73 years, the radiation intensity at 5.9 keV of the calibration sources is required to be more than 0.9 counts/sec/CCD at the BOL in order that the intensity of more than 0.4 counts/sec/CCD is maintained throughout the effective mission lifetime of three years.

3.1.2 CCD chips (PchNeXT4A)

The *XRISM*/SXI employs P-channel Back-Illuminated (BI)-type CCDs with a 200 μm -thick depletion layer, named PchNeXT4A (see §2). Figure 3 shows a photograph of the four flight-model CCD chips mounted on the cold plate, prior to their installation inside SXI-S-HSG. Owing to its thick depletion layer, they achieve a higher Quantum Efficiency (QE) and lower NXB level at around 6 keV than those of the BI-type CCD camera of *Suzaku*/XIS with a 40 μm -thick depletion layer (Koyama et al. 2007). Their charge-transfer architecture is the frame transfer type, and accordingly, each of the CCD chips has an imaging area and a frame-store area. The imaging area has a size of 30.720 mm \times 30.720 mm and 1280 \times 1280 physical pixels. In default, 2 \times 2 on-chip binning is performed first prior to any following processing; as a result, a derived image has 640 \times 640 logical pixels with a pixel size of 48 μm \times 48 μm each. The imaging area and frame-store area are horizontally divided into two segments along the central line of the device, aligned with the columns. The signals from each segment are read out using one of the two readout nodes installed at both ends of the bottom of the frame-store area of each segment. The

CCD operation temperature is -110 or -120°C , either of which is sufficiently low to suppress dark currents to the acceptable level. Table 2 summarizes the specifications of the PchNeXT4A chip.

Nakajima et al. (2018) reported that the most serious concern in the PchNeXT4 chips of *Hitomi*/SXI was optical light leakage. They identified two main paths for leakage: through many pinholes in the Optical Blocking Layer (OBL) and through the physical edges of the chips. Optical leakage caused a significant amount of pseudo-events with the *Hitomi*/SXI in orbit, especially when the base plate of the *Hitomi* spacecraft was pointed to the day Earth, where optical/infrared photons passed through a hole for Extended Optical Bench (EOB) for the Hard X-ray Imager (HXI) and reached the detector surface. The leakage ultimately resulted in a significant reduction in the observation efficiency. To resolve this, we filled the hole of the spacecraft base plate that had been necessary for the HXI in *Hitomi*; this was possible because *XRISM* lacks the HXI unlike *Hitomi*, even though the basic design of *XRISM* follows that of *Hitomi*, including the base plate. Additionally, we directly applied two improvements to the PchNeXT4A chips for the *XRISM*/SXI from PchNeXT4 for the *Hitomi*/SXI to suppress the optical/infrared light leakage. First, we doubled the number of the OBL to reduce the number of pinholes of the X-ray incident surface. As a result, the total thickness of the aluminum layer was increased from 100 nm to 200 nm. Second, we inserted an additional aluminum layer between the bonding sheet and the depletion layer to prevent light leakage from the physical edges of the chips. Figure 4 illustrates the cross-sectional views of PchNeXT4 and PchNeXT4A, highlighting the improved points. Consequently, the optical/infrared blocking performance of the PchNeXT4A chips of the *XRISM*/SXI was confirmed to be significantly improved from the PchNeXT4 chips of the *Hitomi*/SXI, as reported by Uchida et al. (2020).

We applied another improvement, related to the expected degra-

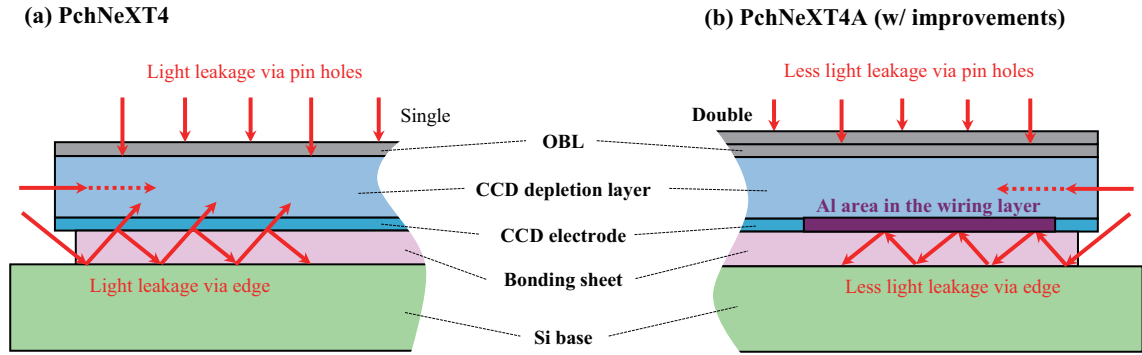


Fig. 4. Schematic illustrations of (left) PchNeXT4 and (right) PchNeXT4a. PchNeXT4A is improved from PchNeXT4 with a doubled OBL and an additional aluminum area between the depletion layer and the bounding sheet (see §3 and Table 1 for detail). Alt text: Two schematic illustrations.

Table 2. Specifications of the CCD chip (PchNeXT4A) for *XRISM/SXI*.

Architecture	Frame Transfer
Channel type	P-channel
Chip size	31.220 mm (horizontal) × 57.525 mm (vertical)
Imaging area size	30.720 mm × 30.720 mm
Pixel format (physical/logical)	1280 × 1280 / 640 × 640
Pixel size (physical/logical)	24 μm × 24 μm / 48 μm × 48 μm
Depletion layer thickness	200 μm (design value)
Incident surface coating	100 nm + 100 nm thick Al (design value)
Readout nodes (equipped/used)	4 / 2
Output	1-stage MOSFET source follower
Charge conversion efficiency	5 μV/e ⁻ (design value)
Readout noise (whole SXI system)	6–7 e ⁻ (rms)

dation of the energy resolution over three years (planned mission lifetime) in orbit, to the PchNeXT4A chips for the *XRISM/SXI*. The degradation is partly the result of the expected increase in the CTI caused by accumulated charge traps in transfer paths in the CCD chips. In addition to the existing charge traps at the time of the launch, it is well known that the number of traps increases in orbit over time due to radiation damage by cosmic rays, which increases the CTI. Since the number of charge transfers varies, depending on the X-ray photon incident positions in the imaging area, the obtained pulse height amplitude for an event of a certain energy of incident photon varies according to the incident position, and its uncertainty increases as the CTI increases over time, which results in degradation of the energy resolution. In order to minimize the CTI increase in orbit, we implanted a narrow notch in the charge transfer path to confine a charge packet to a limited fraction of the pixel width (24 μm) in the PchNeXT4A chips. In fact, Kanemaru et al. (2019) reported that CCD chips with notch implants which are equivalent to the flight-model CCDs showed a ~ 3 times higher radiation hardness than those without them. Thus, we expect a similar improvement in the radiation hardness for PchNeXT4A with our notch implanting.

Furthermore, the charge injection (CI) technique is routinely applied to the *XRISM/SXI* during the operation in orbit to reduce the CTI in the same way as with the *Suzaku/XIS* (e.g., Prigozhin et al. 2008; Nakajima et al. 2008; Uchiyama et al. 2009; Ozawa et al. 2009) and *Hitomi/SXI* (Nobukawa et al. 2014; Tanaka et al. 2018).

The concept is that once CI is conducted, charge traps are filled with artificial charges before charges generated by X-ray events pass the points in order that the potential existent charge traps no longer trap charges from X-ray events. With the *XRISM/SXI*, CI is conducted once per 80 vertical logical-pixel transfers. In each CI, horizontally-aligned artificial charges are injected into the imaging area from the serial register at the top. Figure 5 shows an example of a frame image obtained by one segment of a CCD chip, where CI lines with pulse heights saturated at 4095 ch are confirmed every 80 rows.

3.1.3 Video board

SXI-S-HSG accommodates, in addition to four CCD chips, two video boards, each of which is responsible for processing the front-end signal of two CCD chips (see Figure 1). The main part of the video board consists of two Video Application Specific Integrated Circuits (Video ASICs) named MND02 (Nakajima et al. 2011) and a Video Field-Programmable Gate Array (Video FPGA) with the model number RTAX2000.

The MND02 chips conduct three functions; firstly, it works as a preamplifier of analog signals by a factor of 0.63 to 10 (a factor of 10 is employed in the normal mode), secondly, it performs an analog offset function, and lastly, it does an Analog to Digital (AD) conversion of CCD signals employing the $\Delta-\Sigma$ modulation. In the AD conversion, two modulators are implemented, which work for either of the even and odd columns, to speed up signal pro-

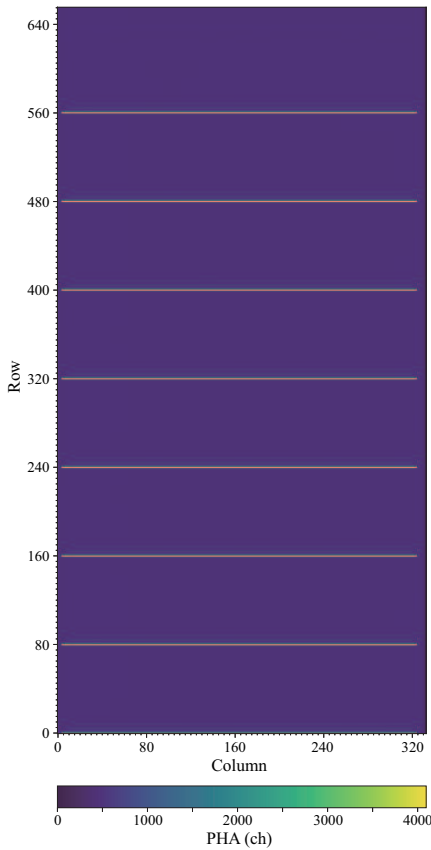


Fig. 5. Frame image obtained from one segment of a CCD chip of the *XRISM/SXI*, with the color scale representing pulse heights (ch). Charge injection (CI) lines saturated at 4095 ch are located every 80 rows. Alt text: One frame image

cessing. We adopted the spare MND02 chips for the *Hitomi/SXI* (Nakajima et al. 2013) as the flight models of the *XRISM/SXI*, the performance and quality of which had been verified to be sufficient for use in orbit.

The Video FPGA performs digital filter processing on the Δ - Σ modulation stream data from the ASICs and converts them into pulse-height data. After the AD conversion, the data of digitized frames are multiplexed and transferred to SXI-PE for subsequent processing. The Video FPGA also controls external interfaces connected to SXI-PE and SXI-S-FE.

3.1.4 Front-end electronics: SXI-S-FE

SXI-S-FE has four driver boards, one for one CCD chip, mounted on SXI-S-BP (Figure 1). The driver board has four main functions. First, it generates bias and clock voltages and supplies them to the CCD chips via the video boards. Second, it measures the CCD temperature and outputs the AD-converted value. Third, it obtains the HK data of the video boards and driver boards, and conducts AD conversion. And fourth, it supplies the power to the heaters on the cold plate, on which the CCD chips are mounted. In pre-flight tests of the *Hitomi/SXI* and monitoring in orbit, we observed occasional events of current anomaly in the driver board when the driver was powered up (Hayashida et al. 2018). We added a countermeasure circuit to SXI-S-FE of the *XRISM/SXI* to suppress the current-anomaly events.

3.1.5 Single stage Stirling cooler: SXI-S-1ST

XRISM/SXI employs a single Stirling cooler manufactured by Sumitomo Heavy Industries, Ltd, named SXI-S-1ST, the model of which is basically the same as that for the *Hitomi/SXI*. A difference is that we installed only one cooler to the *XRISM/SXI*, as opposed to two (equivalent ones) for the *Hitomi/SXI* (Tanaka et al. 2018), because only one is sufficient to cool the CCD temperature to -120 °C. The *Hitomi/SXI* had two for redundancy. We instead installed a dummy cooler in the vacant space.

3.2 Pixel process electronics: SXI-PE

3.2.1 Components and functions of SXI-PE

SXI-PE has one Power Supply Unit (PSU) board and two identical Mission I/O (MIO) boards (Figure 1). The PSU board supplies the DC power to the two MIO boards, the four FE boards, and Video FPGAs in SXI-S from the bus power of the spacecraft. Each MIO board is comprised of two FPGAs, SpaceWire FPGA, User FPGA, and Synchronous Dynamic Random Access Memory (SDRAM). The SpaceWire FPGA controls communications over the SpaceWire. The User FPGA manages functions based on user-specific logic, such as the clock-pattern generation (sequencer) for the CCD driving, processing the CCD data, collecting the HK data from SXI-S-FE, and controlling Digital-Analog Conversions (DACs) on SXI-S-FE. One MIO board provides identical driving patterns to two of the four CCD chips and transmits their data to SXI-DE. To avoid signal interference among the CCD chips, one of the two MIO boards provides a master clock, and both MIO boards share it. The timing signals follow the 10 MHz clock, and thus, the logical levels of individual signals can be assigned in every 0.1 μ sec. Another important function of SXI-PE is the on-board data processing of signals from the SXI-S. This function is summarized in §4.

3.2.2 CCD clocking modes

The timing of CCD-driving voltage clocks and Δ - Σ AD conversions are determined by the microcode programs loaded to SXI-PE, in the same way as used in the *Suzaku/XIS* and *Hitomi/SXI*. The unit times of charge transfer are 14.4 μ sec (69.444 kHz) in the horizontal direction (per logical pixel) and 28.8 μ sec (34.722 kHz) in the vertical direction (per physical pixel). Various clocking modes are available according to the numbers and patterns of horizontal and vertical transfers. Four of the five clocking modes prepared for the *Hitomi/SXI* (Tanaka et al. 2018) are employed for in-orbit observations of the *XRISM/SXI*, where the excluded one is the full-window + 2 sec burst mode.

The four clocking modes of *XRISM/SXI* are described in the following list and in Table 3.

- The “full window + no burst” mode reads out the entire imaging area with an exposure time of 3.96 seconds per image. This mode is used to read out all X-ray events with no spatial or temporal constraints and is called the normal mode.
- The “1/8 window + no burst” mode reads out one-eighth of the imaging area 8 times in 4 seconds with an exposure time of 0.46 seconds per readout. This mode is effective in reducing pile-up effects for bright sources, for which most X-ray events would need to be discarded in the normal mode to reduce the pile-up effects to a similar level.
- The “1/8 window + burst” mode is basically the same as the “1/8 window + no burst” mode except for the exposure time per image of 0.06 seconds, reduced from 0.46 seconds; i.e., this mode reads out signals only after the first 0.06 second exposure

Table 3. Clocking modes of *XRISM*/SXI.

Mode name	Logical pixels (H × V)	Exposure time (sec)	Exposure per frame	Available for guest observers?
Full window + no burst	640 × 640	3.9631	1	Yes
1/8 window + no burst	640 × 80	0.4631	8	Yes
1/8 window + burst	640 × 80	0.0620	8	Yes
Full window + burst	640 × 640	0.0606	1	No

in each frame and reads them blankly in the rest 0.44 seconds. This mode most suppresses the pile-up effects among the four clocking modes and is suitable for observations of the brightest sources.

- The “full window + burst” mode reads out the entire imaging area at 4-sec intervals but limits the exposure time per image to ~ 0.06 sec in a similar way as in the “1/8 window + burst” mode. Whereas this mode highly suppresses pile-up effects caused by a large number of X-ray events when observing bright sources, the dead time is 3.94 seconds per frame, which is over eight times longer than in the “1/8 window + burst” mode. This mode is meant for diagnostic purposes only and is not available for general users of *XRISM*.

3.3 Digital electronics: SXI-DE

SXI-DE is composed of one PSU board and one Central Processing Unit (CPU) board called Space Card (Figure 1). The PSU board supplies DC power to the Space Card from the spacecraft bus power. The Space Card acquires event candidates and frame data extracted by SXI-PE, and performs further data processing, such as event selection. The on-board data processing by SXI-DE is described in §4. After the data processing, SXI-DE converts the event and frame data into telemetry.

Another function of SXI-DE is to serve as the interface between the system of the SXI and the bus system of the spacecraft. SXI-DE receives commands provided by the Satellite Management Unit (SMU) in the bus system of the spacecraft. Conversely, SXI-DE transmits the telemetry of events and the data of HK values to the SMU and the Data Recorder (DR). In addition, SXI-DE oversees the entire SXI system, excluding SXI-S-1ST which is managed by SXI-CD.

3.4 Cooler driver: SXI-CD

Power to operate SXI-S-1ST is supplied by SXI-CD, manufactured by Sumitomo Heavy Industries, Ltd. SXI-CD receives the satellite bus power and generates a sine-wave current to drive the refrigerator compressor and active balancer of SXI-S-1ST. SXI-CD controls the cooler according to the commands received from the SMU. Furthermore, SXI-CD monitors the driving voltage, current, and power of the refrigerator compressor and active balancer and outputs their values as telemetry. In the SXI, SXI-DE regulates the CCD temperature at a target value with the Proportional-Integral-Derivative (PID) control, which increases or decreases the heater current based on its need. Therefore, the SXI-CD does not need or have a temperature sensor for feedback control.

4 Data Processing

The events detected by the CCD chips, both X-ray and non-X-ray events, are processed and screened on board by SXI-PE and

SXI-DE. After the screened event data are downlinked, we correct the pulse height amplitudes on ground in four steps. This section describes the on-board and on-ground data processing and corrections.

4.1 On-board processing

4.1.1 Event candidate extraction in SXI-PE

The CCD analog output is first AD-converted by the video board and then transmitted to SXI-PE, where the data are pre-processed in the UserFPGA. SXI-PE selects designated ASIC channels according to the registered settings and calculates the average values of signals from the readout nodes. Then, SXI-PE estimates the dark level of each pixel, which temporally fluctuates pixel by pixel, and updates it at every frame. Refer to Tanaka et al. (2018) for details on the pixel-by-pixel estimation and updates of the dark level as well as the identification of hot pixels. Subsequently, SXI-PE subtracts the dark level from the raw frame data, and the UserFPGA program identifies X-ray event candidates using the predefined thresholds and relations of pulse-height values in multiple pixels. The raw frame data, dark image (Dark image), pixel-value image (Frame image), event-candidate list, and hot-pixel list are stored in SDRAM. Among them, the Frame image, event candidate list, and hot pixel list are transmitted to SXI-DE for further data processing. Although the event-candidate extraction in SXI-PE is simple, as described above, it improves the efficiency of subsequent processing in SXI-DE.

4.1.2 Event extraction in SXI-DE

The processing in SXI-DE involves several steps. First, the average pulse height of the horizontally overclocked pixel values is subtracted from the pulse heights of imaging-area pixels in every row to exclude short-term variability, which has not been considered in the dark-level calculation at the previous step in SXI-PE. Next, to refine the data further, three filters are applied: the area-discrimination, surround, and 3×3 local-maximum filters. The area-discrimination filtering limits the regions in the imaging area and excludes specified regions from X-ray event searches. The surround filtering removes events with charges distributed over neighboring pixels to eliminate charged-particle background events. The 3×3 local-maximum filtering identifies events with the central pixel in a 3×3 pixel region having a higher pulse height than its eight surrounding pixels. The filtered event data are then transmitted to the DR. In the eventual downlink to ground, the event location, time, and the pulse height of the 5×5 pixels of each event are sent. The data of the inner 3×3 pixel region and outer 16 pixel region of the 5×5 pixel region are separated into distinct packets and may or may not be sent to the ground, depending on the available downlink bandwidth, as they are flagged as lower-priority data. SXI-DE compresses both 3×3 and 5×5 event data to reduce the size of telemetry.

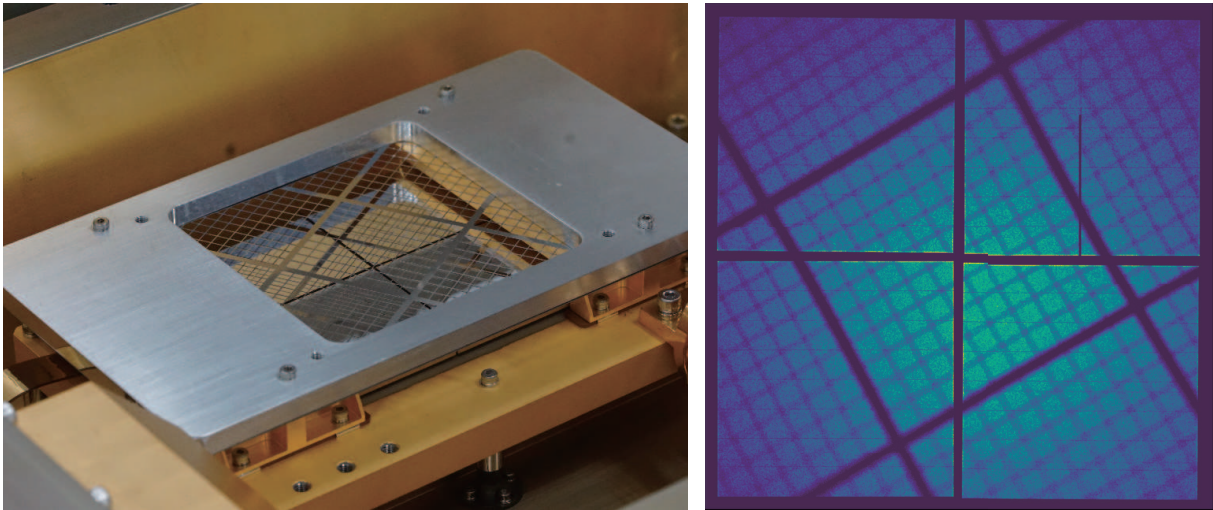


Fig. 6. (Left) Photograph of the mesh mounted on the CCD chips during the SXI stand-alone cooling test. (Right) X-ray image where the entire imaging area is irradiated with Mn-K α photons through the mesh and the orientation between the four CCD chips are adjusted. The distinctive black lines running horizontally and vertically through the center are the CCD chip gaps. The black lines diagonal to the horizontal axis are shadows of the mesh, whereas the thin horizontal and vertical lines are bad columns and those with artificially injected charges with CI, respectively. Alt text: One photograph and one X-ray image.

4.2 Post processing on the ground

4.2.1 Even/Odd correction

As described in §3.1.3, the even and odd columns are independently AD-converted in the signal chain in MND02 on the video board to shorten the processing time. The ASICs for the AD conversions have slightly different gain and offset levels, which lead to a raw image with slightly different pulse-height values and the pedestal (offset) levels between even and odd columns. In addition, Nakajima et al. (2020) found that the gain of the ASICs for the AD conversion is affected by the temperature of the MND02 chip. To address this, we performed a temperature-dependent calibration of the gain and offset levels of the ASICs for the AD conversion after installing the ASICs onto the video boards before the launch of *XRISM*. The calibration result indicates a temperature dependency of approximately 0.1%/20 °C for the flight-model candidate chips, which is incorporated into the calibration database. The temperature-dependent pulse-height difference between the even and odd columns is corrected (called “Even/Odd correction”) during the on-ground pipeline process.

4.2.2 Charge trail and CTI correction

This process addresses the charge loss during a charge transfer. Depending on the trap level depth, timescales of trapping and releasing signal charges vary. In the case of PchNeXT4A, at least three trap populations exist with different timescales (Kanemaru et al. 2020). The shortest timescale is approximately equal to the transfer time of one logical pixel, leading to trailing charges at the pixel next to the event center pixel. The correction for this effect is called the charge-trail correction.

Following the charge-trail correction, the pulse height of each event is corrected according to the CTI with a timescale longer than the transfer period (Kanemaru et al. 2020). This is called the CTI correction. Without the CTI correction, the raw pulse height generally decreases with the number of charge transfers, defined with the formula $PH = PH_0 \times (1 - CTI)^n$, where PH_0 and PH are the pulse height amplitudes before and after charge transfers through n pixels, respectively. Since we employ the CI technique

(see §3.1.2) during operation, the raw pulse height shows a periodic recovery (i.e., a saw-tooth pattern) at the CI rows placed at every 80-th logical row (see §5.2). After the CTI correction, the saw-tooth pattern disappears, and the pulse height becomes independent of the row number. The resultant pulse-height profile is consistent with the expectation in the ideal case without a charge loss during transfer. It is evident that the CTI correction enhances the peak, narrowing the width, in the spectrum of monochromatic X-rays, improving the energy resolution. Since the CTI increases over time due to radiation damage in orbit, the CTI should be recalibrated during the mission. For this purpose, the in-orbit calibration is carried out with onboard calibration-source data and celestial target spectra.

4.2.3 Pulse-height correction based on “grades”

To distinguish between X-ray and particle events, we employ a “grade” method, which classifies grades of events according to the distribution of the pulse height after the charge-trail and CTI corrections. Specifically, For the *XRISM/SXI*, we adopt the same grade selection method as that applied to the *Suzaku/XIS*. The method uses two thresholds: the event threshold and split threshold. If the leakage of the charge cloud to the neighboring pixels of the event-center pixel is smaller than the split threshold, the resultant pulse height is underestimated. This effect is corrected according to the amount of mean expected charge loss for each grade (Aoki et al. 2023).

4.2.4 Gain and line-profile correction

In this step, the corrected pulse height is converted to energy using the response function. The response function is mainly composed of a gain correction and corrections based on the line profile and quantum efficiency. The gain correction converts the corrected pulse height into a final pulse invariant (value calibrated to align the correspondence between pulse height and energy across all CCDs), using the pre-flight calibration data (see §5.2) in such a way that the conversion satisfies the requirement that the difference between the energy calculated from the pulse invariant and

the intrinsic energy fall within 5% at 1 keV and 0.3% at 6 keV. Here, the relation between the pulse invariant value and energy is defined to be $1 \text{ ch} = 6 \text{ eV}$ for the *XRISM/SXI*.

The pulse-height distribution of the CCD events of monochromatic X-rays consists of the following five components.

- Primary Gaussian originating in the events where all the charges generated by incident X-rays are collected.
- Secondary Gaussian originating in the events where the generated charge cloud spreads over multiple pixels and part of the charges are not collected.
- Constant component originating in the events where part of the generated charge cloud spreads outside the depletion layer.
- Si line produced by a Si-K α line or an Auger electron from other pixels.
- Si escape, which is the remainder of the original energy when a Si-K α is emitted and its energy (1.74 keV) is lost accordingly.

See, for example, Inoue et al. (2016) and Tanaka et al. (2018).

We investigated the gain and line profile before the launch by using the data obtained with the multi-color X-ray generator (Yoneyama et al. 2021) and the on-board calibration sources and constructed a response function to account for them. After the launch, the response function is updated with observation data when necessary.

5 Pre-Flight Performance

With extensive pre-flight performance-verification experiments with the full flight configuration of the *XRISM/SXI* or equivalent setups, we confirmed that the *XRISM/SXI* performed at the expected level for the imaging capability (§5.1), spectroscopic performance (§5.2), optical blocking performance (§5.3), cooling and temperature control capabilities (§5.4), and transmissivity and quantum efficiencies (§5.5).

5.1 Imaging capability

To examine the imaging capability of the *XRISM/SXI*, we temporarily installed a mesh frame (Figure 6 left) above the flight-model CCD array, and cooled it to $-110 \text{ }^\circ\text{C}$. We irradiated the entire imaging area with 5.9-keV X-rays from a ^{55}Fe radioisotope source placed above the mesh. In the experiment, the flight-model components of *SXI-S* were used except for *SXI-S-HOOD* and *SXI-S-BNT*. Figure 6 (right) shows the obtained X-ray image. We confirmed that shadows of the mesh were cast over the expected areas while unhindered X-rays were detected in the other areas. No regions on the image were insensitive to X-rays, except for bad columns and those with artificially injected charges with CI. Thus, we confirmed that the *XRISM/SXI* had the expected imaging capability.

The CCD chips are arranged in a 2×2 mosaic configuration to achieve a wider FOV than that with a single chip. The insensitive dead space between devices inevitably exists, and the gap must be precisely characterized. Therefore, we needed to measure the size of these dead spaces. With the imaging experiment with a mesh (Figure 6 (right)), we determined the relative orientation of the four CCD chips. As a result, the gaps between the active pixel regions were found to be $1.2 - 1.6 \text{ mm}$ ($45 - 60''$).

After *XRISM/SXI* and the XMA were mounted on the spacecraft, we checked the alignment between the XMA and *SXI* and confirmed that the on-axis position of the mirror did not fall into the gaps between the CCD chips on ground before the launch.

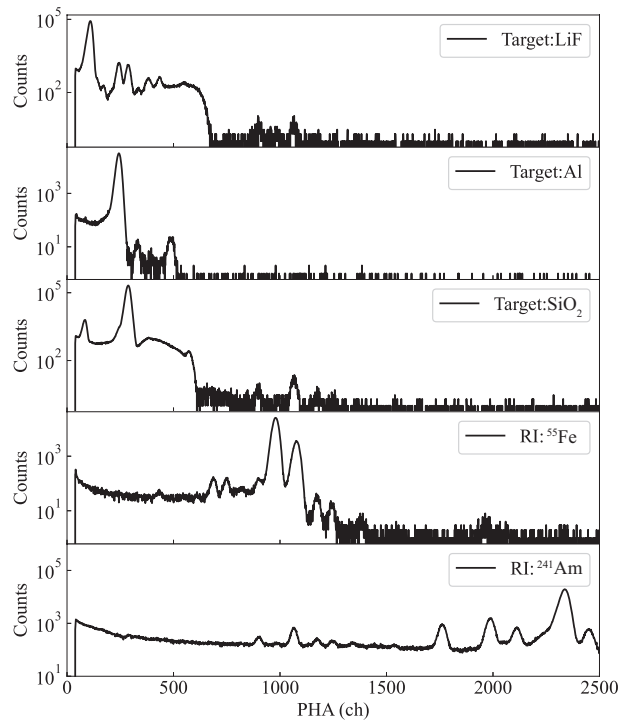


Fig. 7. Spectra obtained in the pre-flight calibration with a multi-color X-ray generator. The horizontal axis is in PHA (ch), where 1000 ch corresponds to $\sim 6 \text{ keV}$. Alt text: Five line graphs.

5.2 Spectroscopic performance

To measure the spectroscopic performance of the flight-model CCD chips at multiple energies, we conducted experiments using a multi-color X-ray generator (Yoneyama et al. 2021). The X-ray generator includes secondary targets of LiF (F-K α at 0.677 keV), Al (Al-K α at 1.49 keV), SiO $_2$ (O-K α at 0.525 keV and Si-K α at 1.74 keV), as well as radioisotopes such as ^{55}Fe (Mn-K α at 5.9 keV) and ^{241}Am (Np-L α at 14.1 keV). In the experiments, we cooled and operated the CCD chips with a non-flight-model read-out system. Figure 7 displays a few example X-ray spectra obtained from five species of targets or radioisotopes. As a representative case, the fourth panel in Figure 7 shows that the Mn-K α and Mn-K β lines from the ^{55}Fe radioisotope were clearly resolved. As such, we confirmed that the *SXI* resolved the emission lines in the range of $\sim 0.5 - 14.1 \text{ keV}$ as expected without a significant loss of the soft X-ray sensitivity.

Next, we changed the configuration to the full flight-model one, and examined the CTI and energy resolution with the ^{55}Fe radioisotope. Figure 8 (left) shows the pulse-height values of Mn-K α and K β as a function of row number in the horizontal direction in a segment of a CCD chip, where the even/odd correction (§4.2.1) was made but not the charge-trail or CTI corrections (§4.2.2). The saw-tooth pattern and the decreasing trend toward higher row numbers in the obtained distribution are due to the lack of the latter two corrections. Figure 8 (right), in contrast, shows the pulse heights where all three corrections were applied. The saw-tooth pattern caused by the lines with CI in every 80 rows (Figure 5) were corrected to some degree, and the pulse-height values of Mn-K α and K β were found to be distributed around constant values, i.e., the systematic trends in Figure 8 (left) were largely eliminated.

After mounting the *XRISM/SXI* to the spacecraft, we tested its

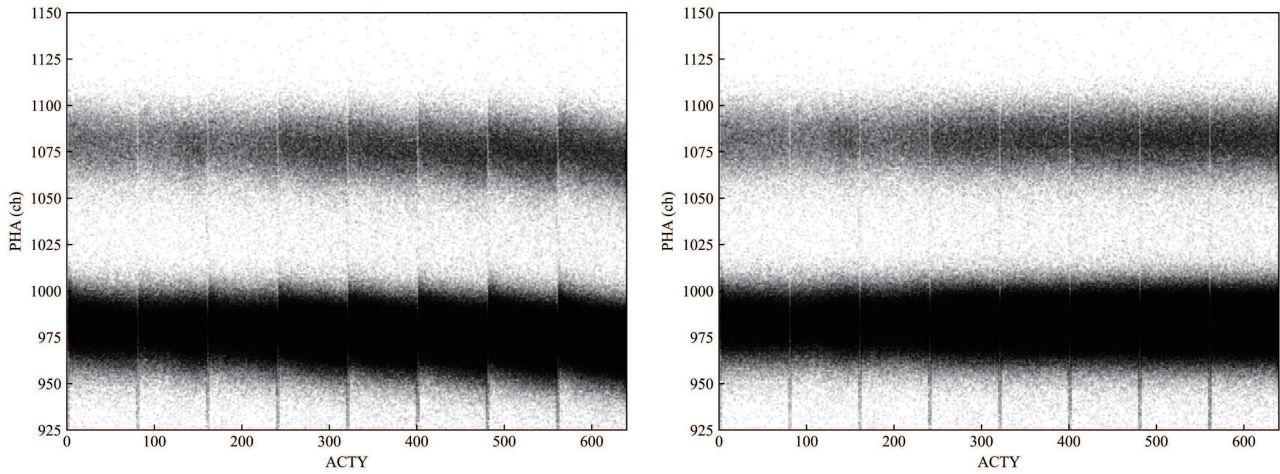


Fig. 8. Pulse heights of Mn- $K\alpha$ and $K\beta$ as a function of row number in the horizontal direction in a segment of a CCD chip. Left and right panels show the pulse heights before and after the charge trail and CTI corrections (§4.2.2) were applied, respectively. Alt text: Two scatter plots.

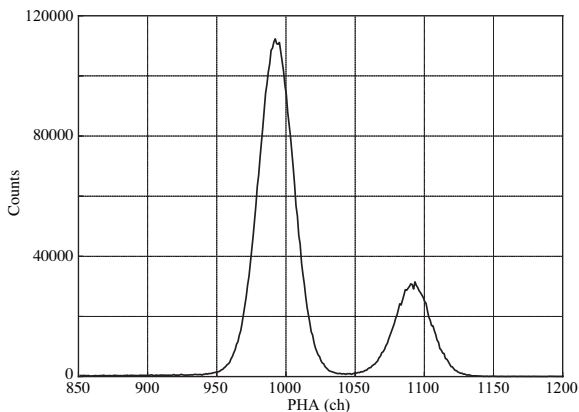


Fig. 9. A spectrum with a Mn- $K\alpha$ and $K\beta$ lines obtained by a segment of a CCD chip of the SXI in the full flight-model configuration. The CCD temperature was kept at -110 °C during the data acquisition. The charge-trail and CTI corrections (§4.2.2) have been applied. Alt text: One line graph.

spectroscopic performance. Figure 9 shows the Mn- $K\alpha$ and $K\beta$ spectra obtained by a segment of a CCD chip with the ^{55}Fe calibration source. We measured the energy resolution at 5.9 keV to be 173 – 188 eV (FWHM), which meets the requirement of < 200 eV (FWHM) at the BOL (see §2). With separate experiments to examine the radiation-damage effects, it has also been demonstrated that the CCD chips should meet the requirement of < 250 eV (FWHM) even after 3 years of operation in orbit (until the EOL), mainly owing to the new notch structure introduced in the CCD chips to reduce the degree of degradation (Kanemaru et al. 2019).

5.3 Optical blocking performance

During the cooling experiments with the flight-model CCDs, we placed a light-emitting diode (LED) near the CCD chips to test the amount of optical light leakage. We found that even the outermost effective pixels, which are most affected by light leakage from the edges, met the light-reduction requirement for the CCD of less

than 10^{-4} . We confirmed that the number of pinhole pixels was less than 1% across the entire surface as we had designed. No significant degradation by aging was observed by Uchida et al. (2020).

After the installation of SXI-S-CBF above SXI-S for the full flight-model configuration, we evaluated the optical blocking performance by irradiating optical photons from LEDs through the SXI-S-CBF. The light leakage was found to be less than 10^{-3} . Consequently, the total light leakage through the SXI-S-CBF and the CCD optical blocking layer was estimated to be less than 10^{-7} , which meets the optical blocking performance requirement.

5.4 Cooling and temperature control capability

After mounting the full-flight configuration of the SXI onto the spacecraft, we continuously operated the SXI-S-1ST and examined the cooling and temperature control capabilities for about one month during the satellite’s thermal vacuum test. In this experiment, the spacecraft was placed in a thermal vacuum chamber, and the environmental temperature was varied to simulate both the cold and hot conditions that the satellite would experience in orbit. The stability of the cooling system and the temperature control of the CCD chips were evaluated in this experiment. Figure 10 shows the long-term temperature history of the four CCD chips during the experiment, along with the camera body temperature², which reflects the environmental temperature. Except for the cooling and warming phases, the CCD temperatures were confirmed to remain stable at the set temperatures of either -110 °C or -120 °C, even though the environmental temperature change was approximately 22 °C. Thus, we successfully verified the sufficient capability of the SXI for cooling and temperature control with the single Stirling cooler system (§3.1.5).

5.5 Detection efficiency

The detection efficiency of the *XRISM/SXI* is defined as a multiplication of the transmissivity of SXI-S-CBF and the quantum efficiency of the CCD chips. The effective area of XtenD is basically

² The temperature was measured at the point between the compressor of SXI-S-1ST and the cooler dummy.

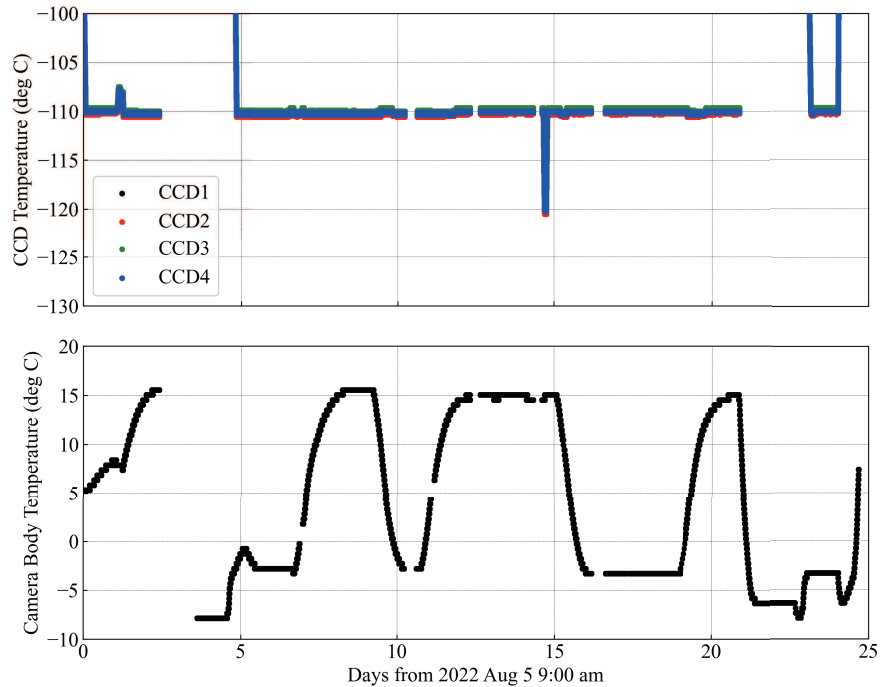


Fig. 10. The long-term history of the temperatures of the (top panel) four CCD chips and (bottom panel) camera body, as a function of days from 9:00 am on 2022 August 5. The camera body temperature reflects the temperature of the surrounding environment of SXI-S. The CCD temperatures first reached -110 °C at 0.07 days. Then, the SXI body was turned at around 1.08 – 1.26 days. The CCDs were warmed up between 2.36 and 4.55 days, and then cooled to -110 °C at 4.85 days. After that, the CCD temperatures were stably kept at -110 °C for ~ 16 days, except for a period from 14.70 to 14.75 days, during which the CCD temperatures were kept at -120 °C. The CCDs were warmed up between 20.87 and 22.84 days and then cooled to -110 °C at 23.18 days. Alt text: Two dotted graphs.

defined as the multiplication of the detection efficiency of the SXI and the effective area of the XMA because X-rays interact with only the XMA and SXI-S-CBF before entering the CCD chips. To evaluate the detection efficiency, we conducted an X-ray beam experiment at the Photon Factory of the High Energy Accelerator Research Organization (KEK), where we separately measured the transmissivity of SXI-S-CBF and the quantum efficiency of the CCD chips. The CBFs used in this experiment were identical to the flight models, except for the absence of a mesh structure with an aperture ratio of 0.896, which supports the structure. The CCD chips used in this experiment were smaller models than the flight models but with structures equivalent to those of the flight models.

Figure 11 (left) shows the measured transmissivity of the SXI-S-CBF as a function of incident energy, along with a (best-fit) model that reproduces the measurements. We also overlay in the figure the model transmissivity curve for the real flight model with the mesh, calculated from the best-fit model and physical parameters of the mesh. The transmissivity for the real flight model was estimated to be 0.857 at 1.5 keV and 0.892 at 6 keV. From the measured transmissivity, we calculated the thicknesses of the Al and polyamide layers to be 102.3 ± 0.5 and 238.2 ± 0.5 nm, respectively, and that of an Al_2O_3 layer to be 7.5 ± 0.5 nm. Figure 11 (right) presents the measured quantum efficiency of the CCD chips, along with a model that reproduces the experimental results. The quantum efficiency of the CCD chips was measured to be 0.957 at 1.5 keV and 0.993 at 6 keV. From the quantum efficiency, the thickness of the Al layer of the CCD chip was estimated to be 230 ± 8 nm under assumptions of the thicknesses of the SiO_2 and Al_2O_3 layers being 20 and 0 nm, respectively. As a result,

we confirmed that both the transmissivity and quantum efficiency meet the requirements to achieve the effective area of Xtend in its specifications, 270 cm² at 6 keV and 300 cm² at 1.5 keV.

6 Conclusion

Xtend is the soft X-ray imaging telescope onboard *XRISM*, which was adopted as a recovery mission for *Hitomi* and whose design is broadly based on that of *Hitomi*. We refined the requirements for Xtend, and accordingly designed and developed the X-ray CCD camera for Xtend, the Soft X-ray Imager (SXI), which covers an energy range of 0.4 – 13.0 keV. This paper presents its design and performance which we verified with pre-flight tests. For the SXI, we employed back-illuminated CCDs with a 200 - μm -thick depletion layer, the same as those onboard *Hitomi*, but with some significant improvements in the optical blocking capability and charge transfer efficiency. The SXI has the 2×2 CCD array and achieves, in combination with the XMA, a large field of view (FOV) of $38' \times 38'$ (large enough to cover the full moon), which encompasses the FOV of the soft X-ray spectroscopy telescope, Resolve, the other instrument of *XRISM*. We conducted pre-flight experiments with the full flight-model configuration of the SXI and confirmed that the imaging capability and spectroscopic performance of the *XRISM*/SXI met expectations and satisfied the requirements for Xtend. We also examined the optical blocking performance, cooling and temperature control capabilities, and detection efficiency of the SXI, using its full flight configuration or equivalent setups, and found that all of them met the requirements. Given

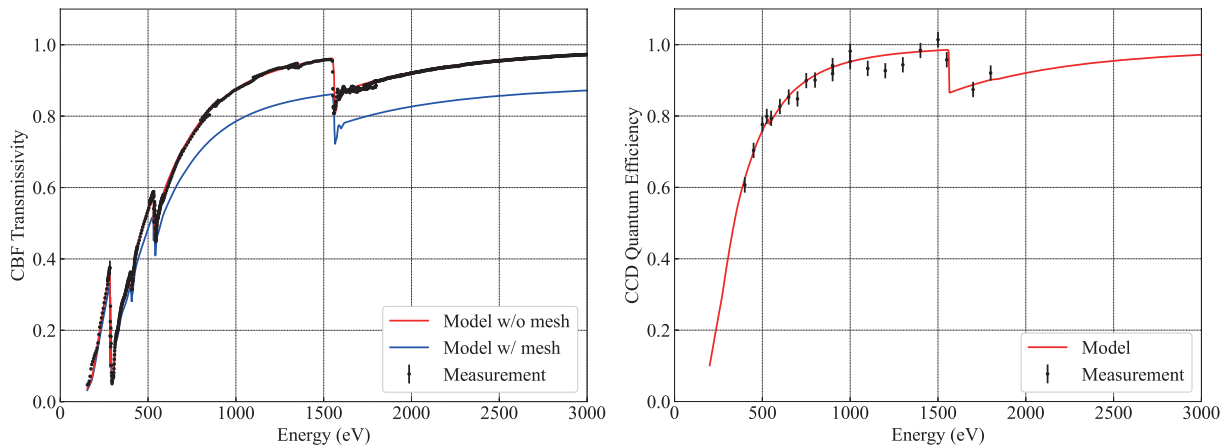


Fig. 11. Model and measured values for the (Left panel) Transmissivity of SXI-S-CBF and (Right panel) quantum efficiency of the CCD chips, as a function of incident energy. Alt text: Two line graphs.

these results, the SXI of *XRISM* can be considered one of the best X-ray CCD cameras onboard X-ray astronomical satellites, in the sense that it has a relatively large FOV with a stable NXB level for a focal-plane X-ray detector, and the combination with the XMA provides the largest grasp at 7 keV among the X-ray CCD cameras onboard large observatories. *XRISM* was successfully launched in 2023, and since then, the SXI, too, has been operated in orbit. The in-orbit performance of Xtend, including whether the effective area and NXB levels meet the requirements, will be reported in a subsequent paper.

Acknowledgments

The authors thank Hiromichi Okon, Takuto Narita, Kai Matsunaga, Yujiro Saito, Moe Anazawa, Hirotake Tsukamoto, Honoka Kiyama, Kaito Fukuda, Mariko Saito, Shuusuke Fudemoto, Satomi Onishi, Junichi Iwagaki, Kazunori Asakura, Maho Hanaoka, Yuichi Ode, Tomohiro Hakamata, Mio Aoyagi, Shunta Nakatake, Toshiki Doi, Kaito Fujisawa, and Mitsuki Hayashida for their contribution to the development of the *XRISM*/Xtend/SXI. This work is supported by Japan Society for the Promotion of Science (JSPS) KAKENHI with the Grant number of 19K21884, 20H01947, 20H01941, 23K20239 (H.N.), 23K20850, 21H01095 (K.M.), 20KK0071, 24H00253 (H.N.), 19K03915, 23K22536, 24K21547 (H.U.), 21J00031, 22KJ3059, 24K17093 (H.S.), 21K03615, 24K00677 (M.N.), 20H00175, 23H00128 (H.M.), 21H04493, 15H02090, 14079204 (T.G.T.), 22H01269 (T.K.), 24K17105 (Y.K.). K. K. N. acknowledges the support by the Yamada Science Foundation.

References

- Aoki Y., Ito Y., Nobukawa M., Kanemaru Y., Miyazaki K., Kusunoki K., Mori K., et al., 2023, *sdpi.conf*, 36
- Hayashida K., Shiroshoji T., Fukuda K., Katayama H., 2003, *SPIE*, 4851, 933. doi:10.1117/12.461500
- Hayashida K., Tomida H., Mori K., Nakajima H., Tanaka T., Uchida H., Tsuru T. G., et al., 2018, *SPIE*, 10699, 1069923. doi:10.1117/12.2311446
- Hitomi Collaboration, Aharonian F., Akamatsu H., Akimoto F., Allen S. W., Anabuki N., Angelini L., et al., 2016, *Natur*, 535, 117. doi:10.1038/nature18627
- Hitomi Collaboration, Aharonian F., Akamatsu H., Akimoto F., Allen S. W., Angelini L., Audard M., et al., 2017, *Natur*, 551, 478. doi:10.1038/nature24301
- Hitomi Collaboration, Aharonian F., Akamatsu H., Akimoto F., Allen S. W., Angelini L., Audard M., et al., 2018, *PASJ*, 70, 9. doi:10.1093/pasj/psx138
- Hitomi Collaboration, Aharonian F., Akamatsu H., Akimoto F., Allen S. W., Angelini L., Audard M., et al., 2018, *PASJ*, 70, 11. doi:10.1093/pasj/psy004
- Hitomi Collaboration, Aharonian F., Akamatsu H., Akimoto F., Allen S. W., Angelini L., Audard M., et al., 2018, *PASJ*, 70, 13. doi:10.1093/pasj/psx147
- Inoue S., Hayashida K., Katada S., Nakajima H., Nagino R., Anabuki N., Tsunemi H., et al., 2016, *NIMPA*, 831, 415. doi:10.1016/j.nima.2016.03.071
- Kanemaru Y., Sato J., Mori K., et al. 2019, *Journal of Instrumentation*, 14, C04003. doi:10.1088/1748-0221/14/04/C04003
- Kanemaru Y., Sato J., Takaki T., Terada Y., Mori K., Saito M., Nobukawa K. K., et al., 2020, *NIMPA*, 984, 164646. doi:10.1016/j.nima.2020.164646
- Koyama, K., Tsunemi, H., Dotani, T., et al. 2007, *PASJ*, 59, 23. doi:10.1093/pasj/59.sp1.S23
- Matsuura D., Ozawa H., Tohiguchi M., Uchino M., Miyata E., Tsunemi H., Inui T., et al., 2006, *JaJAP*, 45, 8904. doi:10.1143/JJAP.45.8904
- Mori K., Tomida H., Nakajima H., Okajima T., Noda H., Tanaka T., Uchida H., et al., 2022, *SPIE*, 12181, 121811T. doi:10.1117/12.2626894
- Mori K., Tomida H., Nakajima H., Okajima T., Noda H., Uchida H., Suzuki H., et al., 2024, *arXiv*, arXiv:2406.19911. doi:10.48550/arXiv.2406.19911
- Nakajima, H., Yamaguchi, H., Matsumoto, H., et al. 2008, *PASJ*, 60, S1. doi:10.1093/pasj/60.sp1.S1
- Nakajima, H., Matsuura, D., Idehara, T., et al. 2011, *Nuclear Instruments and Methods in Physics Research A*, 632, 128. doi:10.1016/j.nima.2010.12.174
- Nakajima, H., Fujikawa, M., Mori, H., et al. 2013, *Nuclear Instruments and Methods in Physics Research A*, 731, 166. doi:10.1016/j.nima.2013.05.146
- Nakajima, H., Maeda, Y., Uchida, H., et al. 2018, *PASJ*, 70, 21. doi:10.1093/pasj/psx116
- Nakajima H., Hayashida K., Tomida H., Mori K., Noda H., Matsumoto H., Yoneyama T., et al., 2020, *SPIE*, 11444, 1144423. doi:10.1117/12.2560348
- Nobukawa K. K., Tsuru T. G., Nobukawa M., Tanaka T., Uchida H., Tsunemi H., Hayashida K., et al., 2014, *NIMPA*, 765, 269. doi:10.1016/j.nima.2014.05.091
- Noda H., Aoyagi M., Mori K., Tomida H., Nakajima H., Tanaka T., Suzuki H., et al., 2024, *SPIE*, 13093, 130935X. doi:10.1117/12.3017877

- Ozawa H., Tohiguchi M., Matsuura D., Miyata E., Tsunemi H., Takagi S., Inui T., et al., 2006, SPIE, 6266, 62662N. doi:10.1117/12.671216
- Ozawa, M., Uchiyama, H., Matsumoto, H., et al. 2009, PASJ, 61, S1. doi:10.1093/pasj/61.sp1.S1
- Prigozhin G., Burke B., Bautz M., Kissel S., Lamarr B., 2008, ITED, 55, 2111. doi:10.1109/ITED.2008.926732
- Takagi S., Tsuru T. G., Inui T., Ozawa M., Matsumoto H., Koyama K., Tsunemi H., et al., 2006, SPIE, 6266, 62663V. doi:10.1117/12.672657
- Takahashi, T., Kokubun, M., Mitsuda, K., et al. 2018, Journal of Astronomical Telescopes, Instruments, and Systems, 4, 021402. doi:10.1117/1.JATIS.4.2.021402
- Tamura K., Hayashi T., Boissay-Malaquin R., Okajima T., Sato T., Olsen L., Koenecke R., et al., 2022, SPIE, 12181, 121811V. doi:10.1117/12.2629534
- Tanaka, T., Uchida, H., Nakajima, H., et al. 2018, Journal of Astronomical Telescopes, Instruments, and Systems, 4, 011211. doi:10.1117/1.JATIS.4.1.011211
- Tashiro M., Maejima H., Toda K., Kelley R., Reichenthal L., Lobell J., Petre R., et al., 2018, SPIE, 10699, 1069922. doi:10.1117/12.2309455
- Tashiro M., Maejima H., Toda K., Kelley R., Reichenthal L., Hartz L., Petre R., et al., 2020, SPIE, 11444, 1144422. doi:10.1117/12.2565812
- Tashiro M., Watanabe S., Maejima H., Toda K., Matsushita K., Yamaguchi H., Kelley R., et al., 2024, SPIE, 13093, 130931G. doi:10.1117/12.3019325
- Uchida, H., Tanaka, T., Amano, Y., et al. 2020, Nuclear Instruments and Methods in Physics Research A, 978, 164374. doi:10.1016/j.nima.2020.164374
- Uchiyama, H., Ozawa, M., Matsumoto, H., et al. 2009, PASJ, 61, S9. doi:10.1093/pasj/61.sp1.S9
- Ueda S., Hayashida K., Nakajima H., Anabuki N., Uchida H., Tsunemi H., Fujikawa M., et al., 2011, SPIE, 8145, 814504. doi:10.1117/12.893348
- Ueda S., Hayashida K., Nakajima H., Anabuki N., Tsunemi H., Kan H., Kohmura T., et al., 2013, NIMPA, 704, 140. doi:10.1016/j.nima.2012.11.187
- Yoneyama T., Noda H., Hanaoka M., Okazaki K., Asakura K., Hayashida K., Ishikura A., et al., 2021, NIMPA, 985, 164676. doi:10.1016/j.nima.2020.164676